

Quantifying gliding forces of filamentous cyanobacteria by self-buckling

Reviewed Preprint

Published from the original preprint after peer review and assessment by eLife.

About eLife's process

Reviewed preprint posted


October 6, 2023 (this version)

Posted to arXiv

April 27, 2023

Sent for peer review

March 22, 2023

Maximilian Kurjahn , Antaran Deka, Antoine Girot, Leila Abbaspour, Stefan Klumpp, Maike Lorenz, Oliver Baumchen, Stefan Karpitschka 

Max Planck Institute for Dynamics and Self-Organization (MPI-DS), Am Faßberg 17, 37077 Göttingen, Germany • Experimental Physics V, University of Bayreuth, Universitätsstr. 30, 95447 Bayreuth, Germany • Max Planck School Matter to Life, University of Göttingen, Friedrich-Hund-Platz 1, 37077 Göttingen, Germany • Institute for Dynamics of Complex Systems, University of Göttingen, Friedrich-Hund-Platz 1, 37077 Göttingen, Germany • Department of Experimental Phycology and SAG Culture Collection of Algae, Albrecht-von-Haller Institute for Plant Science, University of Göttingen, Nikolausberger Weg 18, 37073 Göttingen, Germany

 https://en.wikipedia.org/wiki/Open_access

 Copyright information

Abstract

Filamentous cyanobacteria are one of the oldest and today still most abundant lifeforms on earth, with manifold implications in ecology and economics. Their flexible filaments, often several hundred cells long, exhibit gliding motility in contact with solid surfaces. The underlying force generating mechanism is not yet understood. Here, we demonstrate that propulsion forces and friction coefficients are strongly coupled in the gliding motility of filamentous cyanobacteria. We directly measure their bending moduli using micropipette force sensors, and quantify propulsion and friction forces by analyzing their self-buckling behavior, complemented with analytical theory and simulations. The results indicate that slime extrusion unlikely generates the gliding forces, but support adhesion-based hypotheses, similar to the better-studied single-celled myxobacteria. The critical self-buckling lengths align well with the peaks of natural length distributions, indicating the importance of self-buckling for the organization of their collective in natural and artificial settings.

eLife assessment

This paper describes innovative force measurements of the bending modulus of gliding cyanobacteria, along with measurements of the critical buckling length of the cells, which combined lead to **valuable** insight into how these cells produce the force necessary to move. The major findings are well supported by the data; however, the evidence that the results favor an adhesion-based mechanism is currently **incomplete**.

Filamentous cyanobacteria are an omnipresent group of phototrophic prokaryotes, contributing majorly to the global fixation of atmospheric carbon dioxide. They played an important role already in the paleoclimate of our planet, having generated the atmospheric oxygen [1, 2] on which animal life is based. Today, giant marine and limnic blooms pose ecological and economical threats [1–4], but also enable bioreactor applications, for instance as a renewable energy source [1, 5]. The long and flexible filaments contain up to several hundred, linearly stacked cells. Many species exhibit gliding motility when in contact with solid surfaces or other filaments, but no swimming motion [6]. Motility enables filaments to aggregate into colonies, adapting their architecture to environmental conditions [1, 7]. The force generating mechanism behind gliding is not yet understood [7–16]. Slime extrusion [10], metachronal waves on surface fibrils [8, 13, 17], and acoustic streaming [14] have been proposed. A few species appear to employ a type-IV-pilus related mechanism [7, 16], similar to the better-studied myxobacteria [9, 18–20], which are short, rod-shaped single cells. Yet, most species do not exhibit pili and their gliding mechanism appears to be distinct from myxobacteria [7]. Here we measure the bending moduli of *Kamptonema animale* and *Oscillatoria lutea* (Fig. 1a,b, respectively) by micropipette force sensors [21]. This allows us to quantify the propulsion and friction forces associated with gliding motility, by analyzing their self-buckling behavior. Self-Buckling is an important instability for self-propelling rod-like micro-organisms to change the orientation of their motion, enabling aggregation or the escape from traps [22, 23]. The notion of self-buckling goes back to work of Leonhard Euler in 1780, who described elastic columns subject to gravity [24]. Here, the principle is adapted to the self-propelling, flexible filaments [22, 23] that glide onto an obstacle. Filaments buckle if they exceed a certain critical length $L_c \sim (B/f)^{1/3}$, where B is the bending modulus and f the propulsion force density. By recording numerous collision events, we obtain a comprehensive statistics to derive L_c . Using Kirchhoff beam theory, we derive an analytical expression for the prefactor in L_c and numerically calculate the evolution of the filament shape upon buckling. Comparing experiment with theory, we derive the propulsion force densities and friction coefficients of the living filaments. Force and friction are strongly coupled, which favors an adhesion-based propulsion mechanism [7, 16] over the still customary slime-extrusion hypothesis [10, 11]. The critical lengths we found are close to the peak in the length distribution in freely growing colonies, indicating the importance of this quantity for their self-organization.

Results

Bending measurements.

The bending moduli B of individual filaments of *O. lutea* and *K. animale* were measured by microscopic three-point bending tests [25]. Filaments that glide freely across liquid-immersed surfaces decorated with micro-pillars (SU-8 on glass) were pushed into a gap between two pillars with a Micropipette Force Sensor (MFS, see Fig. 1c). The deflection d of the lever arm of the micropipette is proportional to the load acting on its tip. The corresponding spring constant is obtained from independent calibration measurements (Methods and SI Appendix, Fig. S1a). The base of the pipette was actuated with a constant speed of $\pm 5 \mu\text{m/s}$ to increase and release the force acting on the living filament. Pipette and filament deflections were analyzed with a custom-made image analysis procedure in Matlab (see Methods and [21, 26–28] for details). Fig. 2a shows an exemplary force-displacement curve, accompanied with snapshots from the experiment, for *K. animale*. The measured force-distance relations were continuous, linear, largely speed-independent and free of hysteric effects (SI Appendix, Fig. S1b,c), allowing for an analysis with standard beam theory to derive the effective bending modulus B from the slopes of the force-deflection curves.

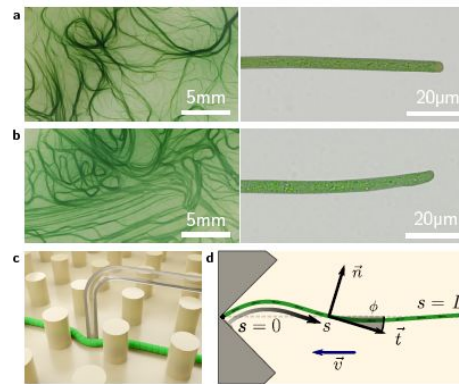


Fig. 1.

Colony and filament morphology of gliding filamentous cyanobacteria, bending and buckling tests.

a, b, Colonies on agar plates (left) and individual filaments in liquid medium (right) of *K. animale* and *O. lutea*, respectively. **c,** Schematic of a microscopic three-point bending test, pushing a filament into the gap between SU-8 pillars using a glass micropipette. **d,** Schematic of a self-buckling test in a microfluidic chip: A filament glides into a V-shaped obstacle and buckles if its contour length L exceeds the self-buckling threshold L_c .

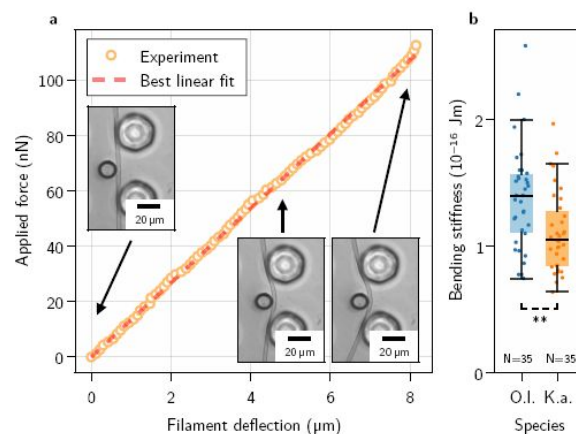


Fig. 2.

Single-filament bending measurements using micropipette force sensors.

a, Representative forcedeflection measurement for *K. animale*. Insets: Bottom-view micrographs of the same experiment. **b,** Box plot of the bending moduli for $N = 35$ individuals of *K. animale* and *O. lutea*, shown as points (each tested 2 – 10 times). Box limits denote the first and third quartile, whiskers the last measurement within the inter-quartile distance away from the respective box limit. A p -value of 6.87×10^{-3} suggests different typical moduli for the two species.

Each individual filament was tested two to ten times at different locations along its contour (see **SI Appendix, Fig. S1d** [for a collection of individual measurements](#)). We observed no systematic dependence of B on the length of the filament or the position along the contour, i.e. no softening or stiffening toward the ends. Stiffness variations on scales below the pillar spacing can of course not be excluded. **Fig. 2b** [shows a box plot of the bending moduli](#). *O. lutea* appears to be slightly stiffer with $B = (1.4 \pm 0.4) \times 10^{-16}$ Jm than *K. animale* with $B = (1.0 \pm 0.3) \times 10^{-16}$ Jm.

Buckling measurements.

We now turn from micropipette bending measurements to self-buckling experiments. The buckling behavior was observed by optical microscopy in quasi-two-dimensional microfluidic compartments filled with liquid medium (**Figs. 1d** [, 3a](#) [and Methods](#)). The height of the chambers was approximately 5 μ , only slightly larger than the diameter of the filaments, such that motion and buckling was confined to the x - y -plane. Filaments explored the entire device and occasionally entered channels that directed them onto V-shaped traps (opening angle 90°). The V-shape is not necessarily required but reduces the chance of filaments slipping sideways instead of buckling, as was observed sometimes for collisions with flat walls. For a collection of collision events with various obstacle architectures, see **SI Appendix, Fig. S2** [. After colliding, the filaments escaped these traps, either by reversing their gliding direction or, if they buckled, due to the reorientation of their front](#). In total, we collected 388 collision events for *O. lutea* and 280 for *K. animale*.

The observed events were classified as **buckling** or **nonbuckling** manually by visual inspection (**Fig. 3a** [and SI Appendix, Fig. S2](#) [. We observed no systematic dependence of the buckling behavior on the shape and size of the trap, nor on the angle of incidence](#). The filament length L as well as the free gliding velocity v_0 prior to hitting the obstacle were determined by automated image processing (Methods). Buckling frequencies (**Fig. 3b,c** [, bars](#)) were evaluated by binning the observations into fixed intervals of the contour length L . Frequently, individual filaments were observed N times, and previous buckling behavior is not readily repeated. Multiple observations of an individual filament were weighted with $1/N$ to obtain an unbiased representation of the population.

The weighted events were analyzed by a logistic regression of the buckling probability

$$p = \text{sig}(x) = (1 + e^{-x})^{-1}, \quad (1)$$

with $x = (L - L_c)/\Delta L_c$. The median critical length L_c and the width of its distribution ΔL_c are obtained by maximum likelihood estimation (Methods). The results are depicted as the dashed curves in **Fig. 3b,c** [. For *O. lutea* we find \$L_c \pm \Delta L_c = \(161 \pm 35\) \mu\text{m}\$ and for *K. animale* \$\(148 \pm 18\) \mu\text{m}\$. The corresponding box plot is shown in **Fig. 3d** \[.\]\(#\)](#)

The substrate contact requires lubrication from polysaccharide slime to enable bacteria to glide [\[7\]](#). Thus we assume an over-damped motion with co-linear friction, for which the propulsion force f and the free gliding velocity v_0 of a filament are related by $f = \eta v_0$, with a friction coefficient η . Thus, since $L_c \sim f^{1/3}$, one may expect also a strong correlation between L_c and v_0 . In order to investigate such a possibility, we include v_0 as a second regressor, by setting $x = (L - L_c(v_0))/\Delta L_c$ in [Eq. \(1\)](#) [, with \$L_c\(v_0\) = \(\eta v_0 / \(30.5722 B\)\)^{1/3}\$, to reflect our expectation from theory \(see below\)](#). **Fig. 3e,f** [show the buckling behavior as color code in terms of the filament length \$L\$ and the free gliding velocity \$v_0\$ prior to hitting the obstacle](#). From maximum likelihood estimation of $L_c(v_0)$ (black lines), we obtain $\eta = (0.6 \pm 0.4) \text{ nN s } \mu\text{m}^{-2}$ for *O. lutea* and $\eta = (0.8 \pm 0.6) \text{ nN s } \mu\text{m}^{-2}$ for *K. animale*. In **Fig. 3g** [we compare \$L_c\(v_0\)\$ for both species, and the results from the one-paramter regression, placed at the mean velocity \$\bar{v}\$.](#)

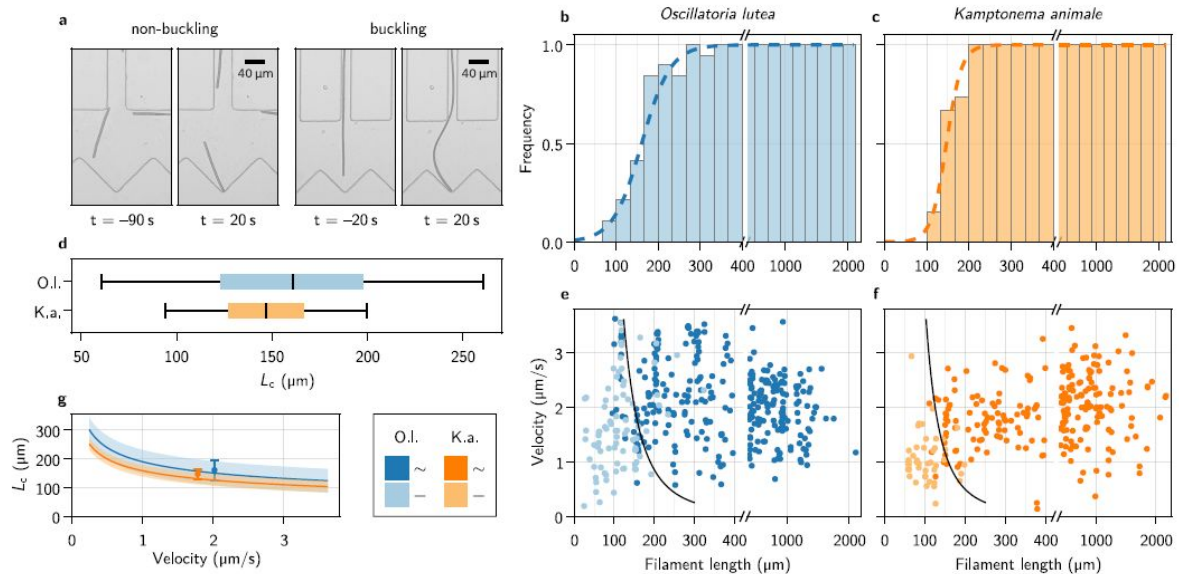


Fig. 3.

Self-buckling experiments and statistics.

a, Snapshots of *K. animale*, before and after hitting the obstacle at $t = 0$. Left, short filament with $L < L_c$, right, long filament with $L > L_c$. b, c, Bar plot of the buckling frequency vs. filament length for *O. lutea* (b, totally $N = 388$ events) and *K. animale* (c, totally $N = 280$ events), together with the logistic regression (dashed curve). d, Box plot of the quantiles of the critical length distribution from the logistic regression $p(L)$. Box limits denote first and third quartile, whiskers the 5th and 95th percentile. e, f, Velocity v_0 immediately before hitting the obstacle vs. filament length L for *O. lutea* and *K. animale*, respectively, distinguishing buckling (\sim , dark) and non-buckling ($-$, light). The velocity-dependent median critical length $L_c(v_0)$, as derived from a logistic regression with L and v_0 as independent explanatory variables, is indicated by black lines. Note that axes in b, c, e, f are broken around $L = 2 L_c$ to emphasize the critical region. g, $L_c(v_0)$ (lines) and inter-quartile region (shaded), together with the simple logistic regression from (d), located at the mean velocity $\overline{v_o}$ of the population (symbols & error bars).

Within the characteristic range of velocities ($1 - 3 \mu\text{ms}^{-1}$), the median L_c depends only mildly on v_0 , as compared to its rather broad distribution, indicated by the bands in **Fig. 3g**. Therefore we conclude that buckling versus non-buckling is mainly governed by the length of a filament, rather than its velocity. Also, we hardly observed short and fast filaments of *K. animale*, which might be caused by physiological limitations [6].

Buckling theory.

In the classical self-buckling theory by Euler, the critical length for a vertical column, clamped at its lower end and free at its upper end, of uniform bending modulus B , subject to a gravitational force density f_g , is given by $L_c = (7.837B/f_g)^{1/3}$ [24]. The buckling of gliding filaments differs in two aspects: the propulsion forces are oriented tangentially instead of vertically, and the front end is supported instead of clamped. Therefore, with $L < L_c$ all initial orientations are indifferently stable, while for $L > L_c$ buckling induces curvature and a resultant torque on the head, leading to rotation [22].

We use classical Kirchhoff theory for a uniform beam of length L and bending modulus B , subject

to a force density $\vec{b} = -f \vec{t} - \eta \vec{v}$ with an effective active force density f along the tangent \vec{t}

, and an effective friction proportional to the local velocity \vec{v} . Presumably, this friction is

dominated by the lubrication drag from the contact with the substrate, filled by a thin layer of secreted polysaccharide slime which is much more viscous than the surrounding bulk fluid. Thus, the drag due to the surrounding bulk fluid can be neglected. We assume a homogeneous and constant distribution of an effectively tangential active force along the filament. Since many cells contribute simultaneously to the gliding force, one may expect noise and fluctuations on the length scale of the individual cell, far below the filament length, which we thus neglect. Based on our observations, we assume a planar configuration and a vanishing twist. Thus we also neglect any helical components of active force or friction, since these appear to merely add rigid-body rotation during free gliding. We parametrize the beam by its orientational angle $\phi(s)$ as a function of the contour coordinate s (see **Fig. 1d**), to obtain the Kirchhoff equation [29]

$$B \partial_s \kappa - \vec{n} \cdot \int_s^L ds' (f \vec{t}(s') + \eta \vec{v}(s')) = 0, \quad (2)$$

with $\kappa = \partial_s \phi$, the curvature and \vec{n} , the unit normal vector. The head of the filament ($s = 0$) is

subject to a localized force \vec{P} that balances the load integral and thereby fixes its position. The tail ($s = L$) is naturally force-free, and the two boundary conditions are vanishing torques at the head and tail of the filament:

$$\kappa|_{s=0} = \kappa|_{s=L} = 0. \quad (3)$$

The local velocity is expressed through

$$\vec{v} = \partial_t \vec{x} = \partial_t \int_0^s ds' \vec{t}(s') = \int_0^s ds' \vec{n}(s') \partial_t \phi(s'). \quad (4)$$

Inserting Eq. (4) into Eq. (2) and changing the order of integration, the inner integral can be evaluated to obtain

$$B \partial_s^2 \phi - \vec{n} \cdot \left\{ \int_s^L ds' \{ f \vec{t} + \eta (L - s') \vec{n} \partial_t \phi \} + \eta (L - s) \int_0^s ds' \vec{n} \partial_t \phi \right\} = 0. \quad (5)$$

Eq. (5) is solved by the method of lines (see Methods and [SI Appendix, Fig. S5](#)).

To derive the critical self-buckling length, [Eq. \(5\)](#) can be linearized for two scenarios that lead to the same L_c : early-time small amplitude buckling and late-time stationary rotation at small and constant curvature [22]. Scaling s by L and t by $t_0 = L^4 \eta / B$, a single dimensionless parameter remains, the activity coefficient $\Gamma = L^3 f / B$. Seeking stationary rotor solutions $\phi(s, t) = \phi(s) + \omega t$, rotating with angular frequency ω , [Eq. \(5\)](#) reduces to (in scaled units)

$$\partial_s^2 \kappa + \Gamma (1 - s) \kappa + \omega s = 0. \quad (6)$$

This second order ordinary differential equation is subject to three boundary conditions,

$\kappa|_{s=0} = \kappa|_{s=1} = \partial_s \kappa|_{s=1} = 0$, hence fixing $\omega(\Gamma)$. The trivial solution $\kappa \equiv 0$ with $\omega = 0$ is amended by a first non-trivial branch of buckled filaments at $\Gamma \approx 30.5722$, the root of a combination of hypergeometric functions which is given in Methods. Thus, in physical units, the critical length is given by $L_c = (30.5722 B / f)^{1/3}$, which is reproduced in particle based simulations ([SI Appendix, Fig. S6](#)).

Inserting the population median of bending modulus and critical length, we can now quantify the active force. We obtain nearly identical values for both species, $f \sim (1.0 \pm 0.6) \text{ nN}/\mu\text{m}$.

Profile analysis.

We will now compare the evolution of theoretical profiles from [Eq. \(5\)](#) to the evolution of the experimental buckling contours. The latter were extracted from the micrographs with an in-house trained convolutional neural network with modified U-Net architecture [30] (see [Fig. 4a](#), green contour) and tracked from the moment of impact until parts other than the head made contact with the confining walls. This limitation narrows down the available data substantially because buckling frequently induced contact with the channel walls. [Fig. 4a](#) shows a representative time series of a buckling filament, together with the extracted contour and the fitted solution of [Eq. \(5\)](#) (see Methods for details of the fitting procedure). From the fit we calculate f and η of individual filaments, using the median bending modulus of the respective species ([Fig. 4c,d](#)). The dashed line on each panel indicates the value from the logistic regression, representative of the population. Filaments below the critical length do not buckle and no values can be derived from profile fitting; this region is indicated in gray. The light gray zone corresponds to the central quartiles of the critical length distribution, where data are biased toward larger forces because only part of the population can buckle. Indeed, here we record the strongest filaments. This bias is not present in the logistic regression, which is most sensitive in the transition region but equally accounts for buckling and non-buckling outcomes.

Discussion

Remarkably, the median active forces for the two species match almost perfectly. The logistic regression gives a good estimate for the population average, and the distributions derived from individual profile fits are centered around this median. The similarity between the two species

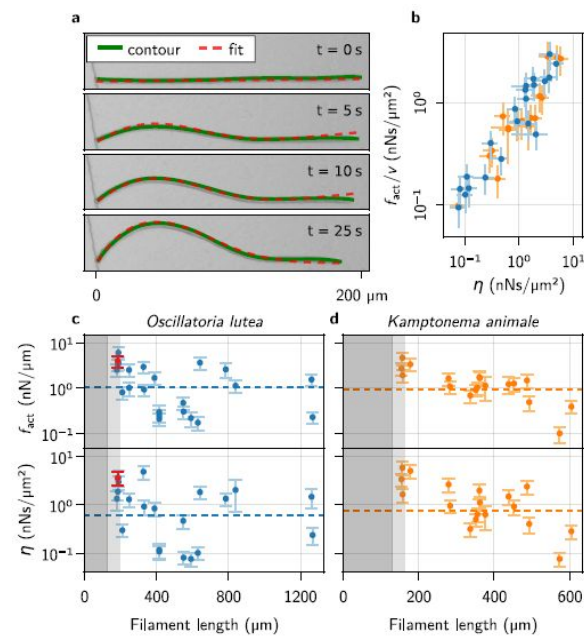


Fig. 4.

Kirchhoff theory compared to experimental contours.

a, Time series of a characteristic buckling event of *O. lutea*, overlaying the contour extracted from the images (green) and the best fit of the solution to **Eq. (5)** (red). b, Free-gliding friction coefficient f_{act}/v against η from the buckling profile fit. c, d, f_{act} and η vs. filament length L , as determined from the fit, for *O. lutea* and *K. animale*, respectively. Light gray indicates $L \in L_c \pm \Delta L_c$ (see **Fig. 3d**), dark gray $L < L_c - \Delta L_c$, where buckling is not observed. The dashed lines are obtained from L_c of logistic regression. The filament from a is indicated in red.

indicates a potential homology of their gliding apparatus.

The comparison with Kirchhoff theory allows us to measure active forces and friction coefficients on an individual basis, going beyond the population mean. Thus it allows for a more insightful analysis, correlating, for instance, these values with length and free gliding speeds. We see no significant correlation between L or v_0 and f or η , but the observed values of f and η cover a wide range (**Fig. 4c,d** and **SI Appendix, Fig. S3**). The two estimates of the friction coefficient, from logistic regression and individual profile fits, are measured in (predominantly) orthogonal directions: tangentially for the logistic regression where the free gliding velocity was used, and transversely for the evolution of the buckling profiles. Thus we plot f/v over η in **Fig. 4b**, finding nearly identical values over about two decades. This relation is remarkable in two aspects: On the one hand, it indicates that friction is mainly isotropic. This suggests that friction is indeed governed by lubrication drag from the slime layer in the contact with the substrate, while neither the hydrodynamic drag from the surrounding bulk fluid [23], nor the available power of the gliding apparatus is rate limiting: these would generate strongly anisotropic friction. On the other hand, it indicates that friction and propulsion forces, despite being quite variable, correlate strongly. Thus, generating more force comes, inevitably, at the expense of added friction. For lubricated contacts, the friction coefficient is proportional to the thickness of the lubricating layer [31], and we conjecture active force and drag both increase due to a more intimate contact with the substrate. This supports the argument of **focal adhesion** [18] as the underlying mechanism of the gliding apparatus of filamentous cyanobacteria: more contacts generate more force, but also pull the filament closer to the substrate, thereby increasing friction to the same extent. Force generation by slime extrusion [10], in contrast, would lead to the opposite behavior: More slime generates more propulsion, but also reduces friction. Still we emphasize that many other possibilities exist. One could, for instance, postulate a regulation of the generated forces to the experienced friction, to maintain some preferred or saturated velocity.

Finally we remark that the distribution of L_c aligns well with the peak of natural length distributions (see **SI Appendix, Fig. S4**). Dwelling in soil or as floating aggregates, natural colonies experience less ideal geometries than in our experiments. Nonetheless we expect a similar buckling behavior since gliding requires contact with a surface or other filaments. As a consequence, small changes in the propulsion force density or the length distribution determine whether the majority of the filaments in a colony is able to buckle or not. This, in turn, has dramatic consequences on the exploration behavior and the emerging patterns [32–35]: $(L/L_c)^3$ is, up to a numerical prefactor, identical to the flexure number [33, 36], the ratio of the Péclet number and the persistence length of active polymer melts. Thus, the ample variety of nonequilibrium phases in such materials [32, 34] may well have contributed to the evolutionary success of filamentous cyanobacteria.

Methods

Cell cultivation.

Species *Oscillatoria lutea* (SAG 1459-3) and *Kamptonema animale* (SAG 1459-6) were obtained from The Culture Collection of Algae at Goettingen University and seeded in T175 culture flask with standard BG-11 nutrition solution. The culture medium was exchanged for fresh BG-11 every four weeks. Cultures were kept in an incubator with an automated 12 h day (30% light intensity (~20 μ E, 18 °C) and 12 h night (0 % light intensity, 14 °C) cycle, with a continuous 2 h transition. All experiments were performed at a similar daytime to ensure comparable phases in their circadian rhythm. The night cycle began at 11 a.m. so experiments could typically be started in the morning towards the end of the bacteria's day.

Bending measurements.

Rectangular arrays of cylindrical micropillars (base diameter 35 μm and pitch of 80 μm in both directions) were fabricated using standard SU-8 photolithography on transparent glass wafers. A liquid sample chamber was made by placing a rectangular microscope glass slide on top of the pillar-decorated substrate, using an O-ring cut into two pieces as spacers. After filling the chamber with standard BG-11 nutrient solution, a small fragment from the cyanobacterial cultures is introduced into the chamber with a syringe.

As filaments dispersed into the pillar-decorated surface autonomously by their gliding motility, a small region with sparsely distributed individual filaments is chosen for bending measurements. Then, a filament is bent between two pillars (6 orders of magnitude stiffer than the filament) with the nozzle of the L-bent glass micropipette force sensor (spring constant $(9.5 \pm 0.3) \text{ nN}/\mu\text{m}$), mounted on a motorized linear actuator (Newport Corporation, LTA-HS). The speed at which the nozzle moves as well as the amplitude of its displacement is set by the actuator. A detailed procedure for the micropipette fabrication and calibration can be found in [21]. In brief, the micropipette is calibrated by measuring the corresponding cantilever deflection under the applied weight of an evaporating water droplet hanging at the pipette nozzle (see **SI Appendix, Fig. S1a**). The corresponding error on the pipette spring constant is given by the standard deviation after independent subsequent calibration measurements. We note that this calibration method provides the spring constant of the micropipette in the direction of the nozzle, while during the bending measurements, a sideways deflection is used. We assume that the elastic properties of the pipette cantilever are isotropic, and therefore consider the spring constant of sideways deflection to be equal to the calibration direction.

Image sequences of deflections were recorded at $20 \times$ magnification and 40 fps with an Olympus IX-83 inverted microscope and a scientific CMOS camera (PCO Edge 4.2). The images were then analyzed with a custommade image analysis procedure in Matlab, to determine the deflections of the filament and the pipette simultaneously. The deflection of the micropipette is obtained by subtracting the time-dependent position of the piezo controller, which is actuating the base of the pipette, from the nozzle position in the image. The force exerted by the pipette is given by its spring constant and its deflection. We note that no torsion of the micropipette cantilever was observed while bending the filament, thus, we assume that torsional modes do not play a significant role for the micropipette deflection analysis. The obtained data of the applied force and filament deflection results in a linear plot as shown in **Fig. 2a**.

We derived the bending modulus according to standard beam theory, through $B = (\Delta x^3/48) \partial P/\partial d$, where Δx is the distance between the pillars, P is the force provided through the pipette, at the center between the two pillars, and d is the deflection of the filament. Our values are comparable but slightly larger than values recently derived from cross-flow drag experiments [37].

SI Appendix, Fig. S1 shows results for different speeds, increasing and decreasing force, as well as a set of exemplary force-distance curves.

Buckling experiments.

We prepared microfluidic devices according to standard procedures of SU-8 cleanroom photolithography, followed by PDMS-based soft lithography [38], binding the cured PDMS imprints to rectangular glass cover slip by plasma activation (Electronic Diener Pico plasma system, air, 50% exposure, 30 seconds). Prior to binding, two 1 mm holes for flushing the device with BG-11 medium, and one 2 mm hole for loading cyanobacteria to the device, were punched in the PDMS, keeping the punch-outs for sealing the chip later on. Four different device architectures, each with 20 μm and 40 μm wide channels, with heights of $\sim 5 \mu\text{m}$ were used.

The devices were first flushed with approximately 5 μL of conditioned BG-11 medium, through one of the small ports. Then, about 1 mm^3 of blue-greenish cyanobacteria were loaded to the device through the large port. Finally, the device was sealed with the cylindrical stoppers retained from the punching, and covered by a small round cover slip to minimize evaporation from the device during the experiment.

Buckling experiments were observed by a Nikon Ti2-E inverted microscope on a passive anti-vibration table, with transmitted illumination at about 20 μE illumination intensity. Microscopy images were taken at 6x- or 10x-magnification with time intervals of either 1 s, 10 s and 30 s for a couple of hours at a resolution of 4096×4096 pixels with a CMOS camera (Dalsa Genie Nano XL).

Image analysis of buckling events.

Regions of interest were cropped from the image sequences for each of the manually detected collision events, from 50 s before to 50 s after the collision, and analyzed further. The length of each filament was obtained by manually adding a path on top of the images in a standard image editor (Gimp). The decision whether a filament buckles or not is made manually by watching the video of each event. The velocity is determined by extracting the position of the head of a filament prior to hitting the obstacle for up to six snapshots, and taking the mean traveled distance over this period.

Profiles were extracted only for selected events in which no additional collisions of the filament with the confining walls were observed for at least ten seconds after the first contact of the head with the obstacle. First, the microscopy images were processed by an in-house trained, modified U-Net to detect their mid-lines (countours). These contour representations of the images were then vectorized into subpixel-accurate x-y-coordinates, to obtain the green contour from [Fig. 4a](#).

Logistic regression.

We perform a logistic regression on the individual (weighted) buckling events with a maximum likelihood estimation. This classification algorithm approximates the probability distribution by a logistic function; see [Eq. \(1\)](#). By maximizing the loglikelihood, we find the parameters that best predict the buckling probability. The likelihood of correctly predicting the buckling ($y = 1$) or non-buckling ($y = 0$) behavior of a filament of known length L is given by

$$P(y|L) = \left[\text{sig} \left(\frac{L - L_c}{\Delta L_c} \right) \right]^y \cdot \left[1 - \text{sig} \left(\frac{L - L_c}{\Delta L_c} \right) \right]^{1-y}, \quad (7)$$

with two parameters L_c and ΔL_c that describe the median critical length and the width of the distribution, respectively. Each individual i with length L_i is observed N_i times to determine the buckling outcomes $y_{i,j}$. The log-likelihood for representing all the data by a logistic distribution is then given by

$$\begin{aligned} \log \mathcal{L}(L_c, \Delta L_c) = & \sum_{i,j} \frac{y_{i,j}}{N_i} \log \text{sig} \left(\frac{L_i - L_c}{\Delta L_c} \right) \\ & + \frac{1 - y_{i,j}}{N_i} \log \left[1 - \text{sig} \left(\frac{L_i - L_c}{\Delta L_c} \right) \right], \end{aligned} \quad (8)$$

where the weight of each observation is given by $1/N_i$, the number of observations of individual i , to yield an unbiased estimate for the subsample of the population. Maximal L requires vanishing derivatives of $\log L$ with respect to the parameters L_c , ΔL_c . For the regression with two explanatory variables L and v_0 i.e., $L_c(v_0) = (\alpha v_0)^{-1/3}$, the same procedure is used, adding the derivative with respect to α to the minimization criteria.

Numerics and fitting.

The evolution of the contour shapes according to [Eq. \(5\)](#) was derived for 30 different values of Γ , ranging from just above the critical length up to $L/L_c \sim 9$, by a numerical solution of [Eq. \(5\)](#). [Eq. \(5\)](#) was discretized into $n = 64$ segments, defining the discrete φ_i on the midpoints of the intervals. Second order polynomial interpolation was then used to evaluate differential and integral terms. Time integration was performed with the method of lines, initialized with a solution to the linearized small-amplitude equation. Snapshots of the solution were stored for 64 times, ranging from small amplitude to head angles $\varphi(s = 0) \sim 90^\circ$. These profiles were linearly interpolated in s and t to obtain a continuous function for fitting to the experimental contours.

As the residual for fitting theoretical profiles to the experiments, we used the square distance between the experimental and theoretical profiles, integrated along the contour. The activity coefficient Γ and time scale t_0 , together with a rotational and two translational degrees of freedom, were then adapted to minimize the sum of the residuals. First the theoretical profile with the smallest mean square distance is determined individually for each frame in an experimental time series, with simulation time, L_c , rotation, and translation as free parameters. The average over these individual fit results were then used as initial parameters for a global fit, where the sum of the residuals of all time steps was minimized simultaneously to derive a global parameter set, containing the time scale t_0 , a time offset, the critical length L_c , rotation, and translation. In order to estimate the error of the fit, we applied a very coarse bootstrapping, repeating the fit 20 times with randomly chosen subsets of the time steps.

For molecular dynamics simulations of buckling, the filaments were discretized as chains of N beads of with diameter σ and a distance $\sigma/2$ between consecutive beads. Flexibility is implemented

with a harmonic bending potential, $U_b = \frac{\kappa b}{2} \sum_{j=2}^{N-1} (\theta_j - \pi)^2$, where θ_j is the angle between

consecutive beads $i - 1$, i , $i + 1$, and self-propulsion by an active force F_a on each bead, oriented tangentially along the chain [\[32\]](#). The parameters κ_b and f_a are related to the measured parameters B and f via $B \approx \sigma \kappa_b / 2$ and $f \approx 2 F_a / \sigma$. Buckling is induced by steric interaction using a WCA potential [\[32\]](#) with a V-shaped obstacle. The dynamics of the chain is given by an overdamped Langevin equation and simulated with the molecular dynamics software HOOMD-blue [\[39\]](#).

Critical length.

To derive an analytical expression for the critical Γ in [Eq. \(6\)](#), we first solve the homogeneous equation by

$$\kappa_{\omega=0} = c_1 \text{Ai} \left(k^{1/3} r \right) + c_2 \text{Bi} \left(k^{1/3} r \right), \quad (9)$$

with $r = s - 1$, and give a particular solution to the inhomogeneous equation:

$$\begin{aligned} \kappa = \kappa_{\omega=0} + \frac{1}{k} - r^2 \\ \cdot \left({}_0F_1 \left(\frac{4}{3}; \frac{k}{9} r^3 \right) {}_1F_2 \left(\frac{1}{3}; \frac{2}{3}, \frac{4}{3}; \frac{k}{9} r^3 \right) \right. \\ \left. - \frac{1}{2} {}_0F_1 \left(\frac{2}{3}; \frac{k}{9} r^3 \right) {}_1F_2 \left(\frac{2}{3}; \frac{4}{3}, \frac{5}{3}; \frac{k}{9} r^3 \right) \right), \end{aligned} \quad (10)$$

where the ${}_pF_q$ are the generalized hypergeometric functions. The parameters c_1 and c_2 are determined by the torque boundary conditions. Then, Γ is found from the remaining force boundary condition, which boils down to the roots of

$$2k {}_0F_1\left(\frac{4}{3}; -\frac{k}{9}\right) {}_1F_2\left(\frac{1}{3}; \frac{2}{3}, \frac{4}{3}; -\frac{k}{9}\right) + {}_0F_1\left(\frac{2}{3}; -\frac{k}{9}\right) \left\{2 - k {}_1F_2\left(\frac{2}{3}; \frac{4}{3}, \frac{5}{3}; -\frac{k}{9}\right)\right\} = 2. \quad (11)$$

The smallest root is $k \approx 30.5722$.

Acknowledgements

The authors gratefully acknowledge the Algae Culture Collection (SAG) in Göttingen, Germany, for providing the cyanobacteria species ***O. lutea*** (SAG 1459-3) and ***K. animale*** (SAG 1459-6), and technical support. We also thank D. Struover, M. Benderoth, W. Keiderling, and K. Hantke for technical assistance, culture maintenance, and discussions. We further thank D. Qian for assistance with the microfluidic devices. The work of L. A. and S. Kl. was done within the Max Planck School Matter to Life, supported by the German Federal Ministry of Education and Research (BMBF) in collaboration with the Max Planck Society. We gratefully acknowledge discussions with M. Prakash, R. Golestanian, A. Vilfan, K. R. Prathyusha, and F. Papenfuß.

Supplementary Material

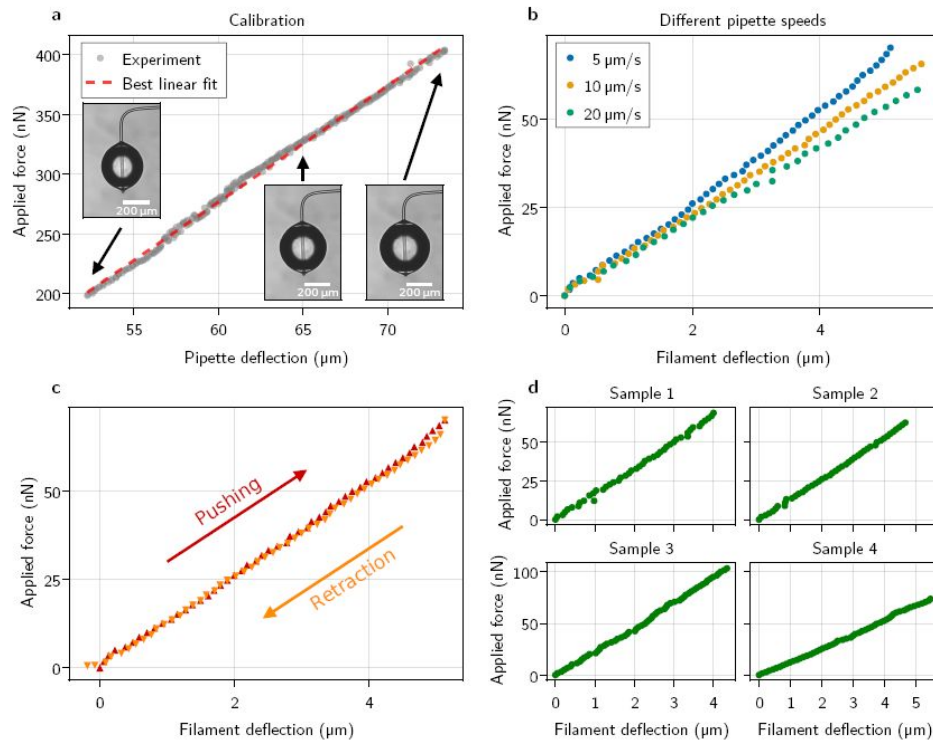


Fig. S1.

Details on the microscopic three-point bending tests. a, Calibration of the force sensing micropipette by the weight of an evaporating water droplet. b, Testing the same filament with three different actuation speeds shows a negligible speed-dependence of the force distance curves as compared to the spread between individual measurements. c, Force-distance curves for increasing ('pushing') and decreasing ('retraction') deflection, showing the absence of hysteresis. d, Force-distance measurements for four individual filaments of *K. animale*.

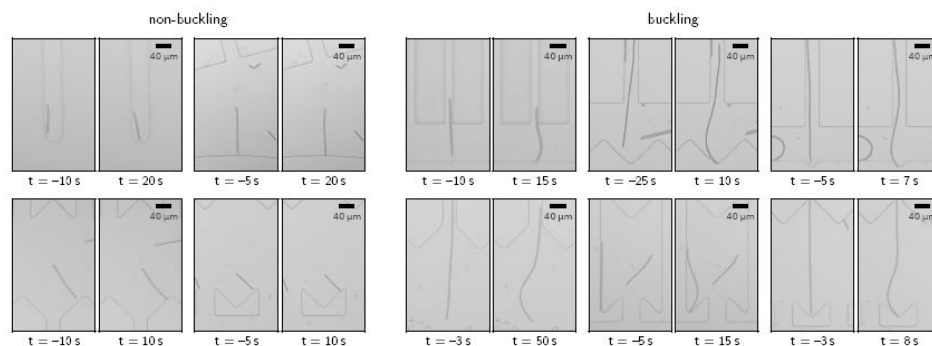


Fig. S2.

Collection of buckling events with different shapes of the traps. Snapshots of *K. animale* (top row) and *O. lutea* (bottom row), before and after hitting the obstacle at time $t = 0$. Left, four short filaments with length below the critical length, right, six long filaments above the critical length.

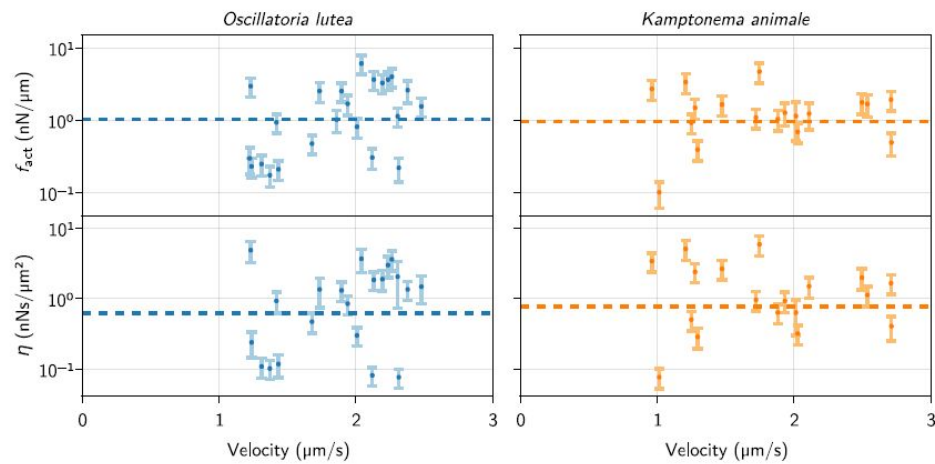


Fig. S3.

Active force f_{act} and friction coefficient η vs. filament velocity. Velocities were measured immediately before hitting the obstacle. Neither f_{act} nor η appears to be correlated with the velocity.

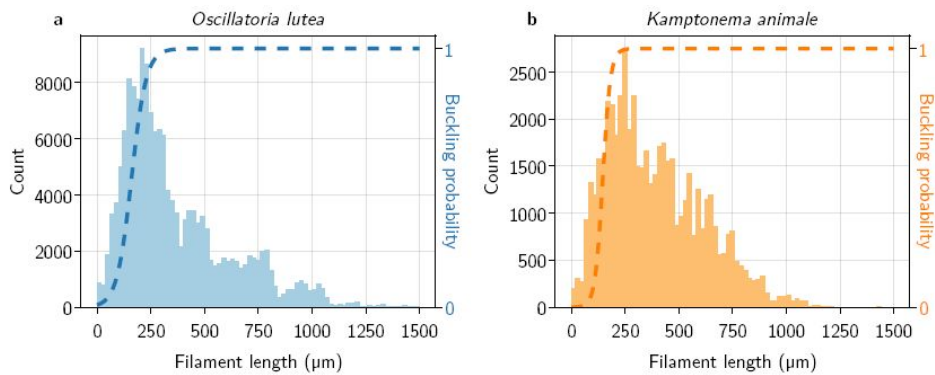


Fig. S4.

Length distributions of *K. animale* and *O. lutea*, together with the buckling probability estimated by the logistic regression. Colonies were grown in quiescent liquid medium and then gently squeezed in between agar solidified medium and glass. Filaments glide from the colony into the glass-agar contact and form a sub-monolayer. After ~ 6 h, the layer is then analyzed by our modified U-Net segmentation procedure. Filaments remain intact and alive in this configuration for days, as inferred from their gliding velocity.

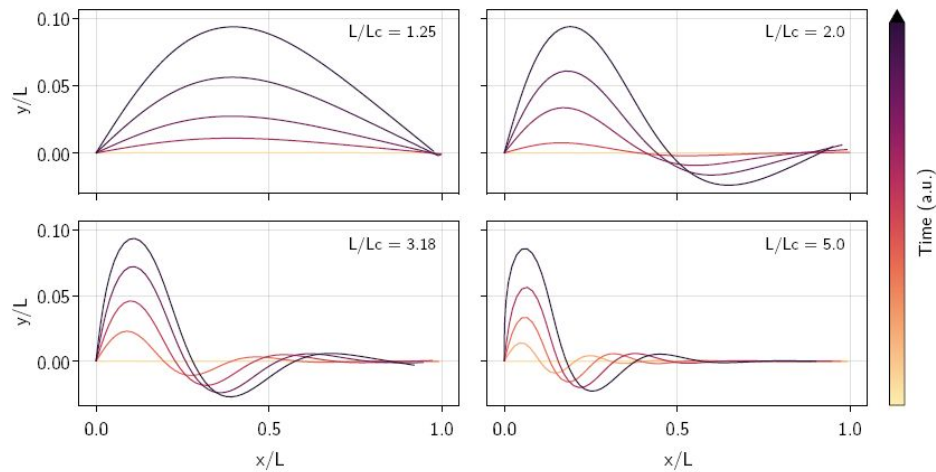


Fig. S5.

Numerical results for the full non-linear Kirchhoff theory. Eq. (5) is discretized according to the scheme described in Methods and integrated over time, starting from a small-amplitude analytical solution to the linearized equations.

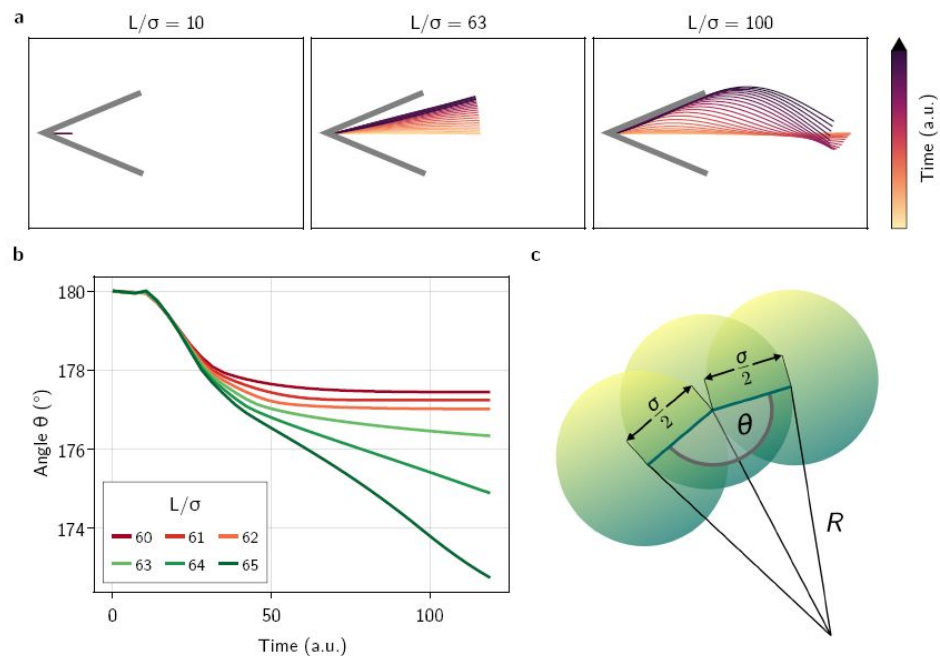


Fig. S6.

Simulations of self-buckling semi-flexible chains of active overdamped particles. Chains of particles of diameter σ and separation $\sigma/2$ are connected by torsional springs to generate an effective bending modulus. Each particle self-propels along the tangent of the particle chain, defined by the mean orientation of its two bonds. a, Trajectory of active particle chains of 21, 127 and 201 particles, corresponding to filament lengths L of 10σ , 63σ and 100σ , respectively. b, Front-Mid-End angle of particle chains as a function of time, after hitting the obstacle. Active force and torsional spring constant were chosen to obtain, from the analytical expression, $L_c \sim 62.37$. The chain hits the obstacle slightly off-center, to induce a non-singular initial condition for self-buckling. For $L < L_c$ (red colors), curvature stagnates and then relaxes very slowly. For $L > L_c$ (green colors), curvature increases further. c, Definition of the Geometry of the particle chains.

References

- [1] Whitton B. A. (2012) **Ecology of Cyanobacteria II**
- [2] Sciuto K., Moro I. (2015) **Cyanobacteria: the bright and dark sides of a charming group** *Biodiversity and Conservation* **24**
- [3] Bauer F., Fastner J., Bartha-Dima B., Breuer W., Falkenau A., Mayer C., Raeder U. (2020) **Mass occurrence of anatoxin-a- and dihydroanatoxin-a-producing tychonema sp. in mesotrophic reservoir mandichosee (river lech, germany) as a cause of neurotoxicosis in dogs** *Toxins* **12**
- [4] Fastner J. *et al.* (2018) **Fatal neurotoxicosis in dogs associated with tycho planktic, anatoxin-a producing tychonema sp. in mesotrophic lake tegel, berlin** *Toxins* **10**
- [5] Ruffing A. M., Kallas T. (2016) **Cyanobacteria: The Green E. coli**
- [6] Burkholder P. R. (1934) **Movement in the cyanophyceae**, *The Quarterly Review of Biology* **9**
- [7] Khayatan B., Meeks J. C., Risser D. D. (2015) **Evidence that a modified type IV pilus-like system powers gliding motility and polysaccharide secretion in filamentous cyanobacteria** *Mol. Microbiol* **98**
- [8] Halfen L. N., Castenholz R. W. (1971) **Gliding motility in the blue-green alga oscillatoria princeps** *J. Phycol* **7**
- [9] Godwin S. L., Fletcher M., Burchard R. P. (1989) **Interference reflection microscopic study of sites of association between gliding bacteria and glass substrata** *J. Bacteriol* **171**
- [10] Hoiczky E., Baumeister W. (1998) **The junctional pore complex, a prokaryotic secretion organelle, is the molecular motor underlying gliding motility in cyanobacteria** *Curr. Biol* **8**
- [11] McBride M. J. (2001) **Bacterial gliding motility: Multiple mechanisms for cell movement over surfaces** *Annu. Rev. Microbiol* **55**
- [12] Gupta S., Agrawal S. (2006) **Motility in oscillatoria salina as affected by different factors** *Folia Microbiol* **51**
- [13] Read N., Connell S., Adams D. G. (2007) **Nanoscale visualization of a fibrillar array in the cell wall of filamentous cyanobacteria and its implications for gliding motility** *J. Bacteriol* **189**
- [14] Koiller J., Ehlers K. M., Chalub F. (2010) **Acoustic streaming, the “small invention” of cyanobacteria?** *Arbor* **186**
- [15] Hanada Y., Sugioka K., Shihira-Ishikawa I., Kawano H., Miyawaki A., Midorikawa K. (2011) **3d microfluidic chips with integrated functional microelements fabricated by a femtosecond laser for studying the gliding mechanism of cyanobacteria** *Lab. Chip* **11**
- [16] Wilde A., Mullineaux C. W. (2015) **Motility in cyanobacteria: polysaccharide tracks and type IV pilus motors** *Mol. Microbiol* **98**

- [17] Halfen L. N. (1973) **Gliding motility of oscillatoria: Ultrastructural and chemical characterization of the fibrillar layer** *J. Phycol* **9**
- [18] Mignot T., Shaevitz J. W., Hartzell P. L., Zusman D. R. (2007) **Evidence that focal adhesion complexes power bacterial gliding motility** *Science* **315**
- [19] Nan B., McBride M. J., Chen J., Zusman D. R., Oster G. (2014) **Bacteria that glide with helical tracks** *Curr. Biol* **24**
- [20] Copenhagen K., Alert R., Wingreen N. S., Shaevitz J. W. (2021) **Topological defects promote layer formation in myxococcus xanthus colonies** *Nature Physics* **17**
- [21] Backholm M., Bäumchen O. (2019) **Micropipette force sensors for in vivo force measurements on single cells and multicellular microorganisms** *Nat. Protoc* **14**
- [22] Fily Y., Subramanian P., Schneider T. M., Chelakkot R., Gopinath A. (2020) **Buckling instabilities and spatiotemporal dynamics of active elastic filaments** *Journal of The Royal Society Interface* **17**
- [23] Man Y., Kanso E. (2019) **Morphological transitions of axially-driven microfilaments** *Soft Matter* **15**
- [24] Elishakoff I. (2000) **A closed-form solution for the generalized euler problem** *Proc. R. Soc. Lond. A* **456**
- [25] Backholm M., Ryu W. S., Dalnoki-Veress K. (2013) **Viscoelastic properties of the nematode caenorhabditis elegans, a self-similar, shear-thinning worm** *Proc. Natl. Acad. Sci. USA* **110**
- [26] Kreis C. T., Le Blay M., Linne C., Makowski M. M., Bäumchen O. (2017) **Adhesion of chlamydomonas microalgae to surfaces is switchable by light** *Nat. Phys* **14**
- [27] Kreis C. T., Grangier A., Bäumchen O. (2019) **In vivo adhesion force measurements of chlamydomonas on model substrates** *Soft Matter* **15**
- [28] Boddeker T. J., Karpitschka S., Kreis C. T., Magdelaine Q., Baumchen O. (2020) **Dynamic force measurements on swimming chlamydomonas cells using micropipette force sensors** *J. R. Soc. Interface* **17**
- [29] Audoly B., Pomeau Y. (2018) **Elasticity and Geometry: From hair curls to the non-linear response of shells**
- [30] Ronneberger O., Fischer P., Brox T. (2015) **U-net: Convolutional networks for biomedical image segmentation** *International Conference on Medical image computing and computer-assisted intervention* :234–241
- [31] Snoeijer J. H., Eggers J., Venner C. H. (2013) **Similarity theory of lubricated hertzian contacts** <https://doi.org/10.1063/1.4826981>
- [32] Abbaspour L., Malek A., Karpitschka S., Klumpp S. (2021) **Effects of direction reversals on patterns of active filaments** *arXiv 2112.09188v1*
- [33] Duman O., Isele-Holder R. E., Elgeti J., Gompper G. (2018) **Collective dynamics of self-propelled semiflexible filaments** *Soft Matter* **14**

- [34] Prathyusha K. R., Henkes S., Sknepnek R. (2018) **Dynamically generated patterns in dense suspensions of active filaments** *Physical Review E* **97** <https://doi.org/10.1103/physreve.97.022606>
- [35] Jung W., Fillenwarth L. A., Matsuda A., Li J., Inoue Y., Kim T. (2020) **Collective and contractile filament motions in the myosin motility assay** *Soft Matter* **16**
- [36] Winkler R. G., Elgeti J., Gompper G. (2017) **Active polymers — emergent conformational and dynamical properties: A brief review** *J. Phys. Soc. Jpn* **86**
- [37] Faluweki M. K., Goehring L. (2022) **Structural mechanics of filamentous cyanobacteria**
- [38] Fujii T. (2002) **Pdms-based microfluidic devices for biomedical applications** *Microelectronic Engineering* **61**
- [39] Anderson J. A., Glaser J., Glotzer S. C. (2020) **Hoomd-blue: A python package for high-performance molecular dynamics and hard particle monte carlo simulations** *Computational Materials Science* **173**

Article and author information

Maximilian Kurjahn

Max Planck Institute for Dynamics and Self-Organization (MPI-DS), Am Fassberg 17, 37077 Göttingen, Germany

For correspondence: maximilian.kurjahn@ds.mpg.de

Antaran Deka

Max Planck Institute for Dynamics and Self-Organization (MPI-DS), Am Fassberg 17, 37077 Göttingen, Germany

Antoine Girot

Max Planck Institute for Dynamics and Self-Organization (MPI-DS), Am Fassberg 17, 37077 Göttingen, Germany, Experimental Physics V, University of Bayreuth, Universitätsstr. 30, 95447 Bayreuth, Germany

Leila Abbaspour

Max Planck School Matter to Life, University of Göttingen, Friedrich-Hund-Platz 1, 37077 Göttingen, Germany, Institute for Dynamics of Complex Systems, University of Göttingen, Friedrich-Hund-Platz 1, 37077 Göttingen, Germany

Stefan Klumpp

Max Planck School Matter to Life, University of Göttingen, Friedrich-Hund-Platz 1, 37077 Göttingen, Germany, Institute for Dynamics of Complex Systems, University of Göttingen, Friedrich-Hund-Platz 1, 37077 Göttingen, Germany

Maike Lorenz

Department of Experimental Phycology and SAG Culture Collection of Algae, Albrecht-von-Haller Institute for Plant Science, University of Göttingen, Nikolausberger Weg 18, 37073 Göttingen, Germany

Oliver Baumchen

Max Planck Institute for Dynamics and Self-Organization (MPI-DS), Am Fassberg 17, 37077
Gottingen, Germany, Experimental Physics V, University of Bayreuth, Universitätsstr. 30, 95447
Bayreuth, Germany

Stefan Karpitschka

Max Planck Institute for Dynamics and Self-Organization (MPI-DS), Am Fassberg 17, 37077
Gottingen, Germany

For correspondence: stefan.karpitschka@ds.mpg.de

Copyright

© 2023, Kurjahn et al.

This article is distributed under the terms of the [Creative Commons Attribution License](#), which permits unrestricted use and redistribution provided that the original author and source are credited.

Editors

Reviewing Editor

Pierre Sens

Institut Curie, CNRS UMR168, France

Senior Editor

Aleksandra Walczak

École Normale Supérieure - PSL, France

Reviewer #1 (Public Review):

The paper "Quantifying gliding forces of filamentous cyanobacteria by self-buckling" combines experiments on freely gliding cyanobacteria, buckling experiments using two-dimensional V-shaped corners, and micropipette force measurements with theoretical models to study gliding forces in these organisms. The aim is to quantify these forces and use the results to perhaps discriminate between competing mechanisms by which these cells move. A large data set of possible collision events are analyzed, bucking events evaluated, and critical buckling lengths estimated. A line elasticity model is used to analyze the onset of buckling and estimate the effective (viscous type) friction/drag that controls the dynamics of the rotation that ensues post-buckling. This value of the friction/drag is compared to a second estimate obtained by consideration of the active forces and speeds in freely gliding filaments. The authors find that these two independent estimates of friction/drag correlate with each other and are comparable in magnitude. The experiments are conducted carefully, the device fabrication is novel, the data set is interesting, and the analysis is solid. The authors conclude that the experiments are consistent with the propulsion being generated by adhesion forces rather than slime extrusion. While consistent with the data, this conclusion is inferred.

Summary:

The paper addresses important questions on the mechanisms driving the gliding motility of filamentous cyanobacteria. The authors aim to understand these by estimating the elastic properties of the filaments, and by comparing the resistance to gliding under a) freely gliding conditions, and b) in post-buckled rotational states. Experiments are used to estimate the propulsion force density on freely gliding filaments (assuming over-damped conditions). Experiments are combined with a theoretical model based on Euler beam theory to extract

friction (viscous) coefficients for filaments that buckle and begin to rotate about the pinned end. The main results are estimates for the bending stiffness of the bacteria, the propulsive tangential force density, the buckling threshold in terms of the length, and estimates of the resistive friction (viscous drag) providing the dissipation in the system and balancing the active force. It is found that experiments on the two bacterial species yield nearly identical values of f (albeit with rather large variations). The authors conclude that the experiments are consistent with the propulsion being generated by adhesion forces rather than slime extrusion.

Strengths of the paper:

The strengths of the paper lie in the novel experimental setup and measurements that allow for the estimation of the propulsive force density, critical buckling length, and effective viscous drag forces for movement of the filament along its contour - the axial (parallel) drag coefficient, and the normal (perpendicular) drag coefficient (I assume this is the case, since the post-buckling analysis assumes the bent filament rotates at a constant frequency). These direct measurements are important for serious analysis and discrimination between motility mechanisms.

Weaknesses:

There are aspects of the analysis and discussion that may be improved. I suggest that the authors take the following comments into consideration while revising their manuscript.

The conclusion that adhesion via focal adhesions is the cause for propulsion rather than slime protrusion is consistent with the experimental results that the frictional drag correlates with propulsion force. At the same time, it is hard to rule out other factors that may result in this (friction) viscous drag - (active) force relationship while still being consistent with slime production. More detailed analysis aiming to discriminate between adhesion vs slime protrusion may be outside the scope of the study, but the authors may still want to elaborate on their inference. It would help if there was a detailed discussion on the differences in terms of the active force term for the focal adhesion-based motility vs the slime motility.

Can the authors comment on possible mechanisms (perhaps from the literature) that indicate how isotropic friction may be generated in settings where focal adhesions drive motility? A key aspect here would probably be estimating the extent of this adhesion patch and comparing it to a characteristic contact area. Can lubrication theory be used to estimate characteristic areas of contact (knowing the radius of the filament, and assuming a height above the substrate)? If the focal adhesions typically cover areas smaller than this lubrication area, it may suggest the possibility that bacteria essentially present a flat surface insofar as adhesion is concerned, leading to a transversely isotropic response in terms of the drag. Of course, we will still require the effective propulsive force to act along the tangent.

I am not sure why the authors mention that the power of the gliding apparatus is not rate-limiting. The only way to verify this would be to put these in highly viscous fluids where the drag of the external fluid comes into the picture as well (if focal adhesions are on the substrate-facing side, and the upper side is subject to ambient fluid drag). Also, the friction referred to here has the form of a viscous drag (no memory effect, and thus not viscoelastic or gel-like), and it is not clear if forces generated by adhesion involve other forms of drag such as chemical friction via temporary bonds forming and breaking. In quasi-static settings and under certain conditions such as the separation of chemical and elastic time scales, bond friction may yield overall force proportional to local sliding velocities.

For readers from a non-fluids background, some additional discussion of the drag forces, and the forms of friction would help. For a freely gliding filament if f is the force density (per unit length), then steady gliding with a viscous frictional drag would suggest (as mentioned in the paper) $f \sim \nu! L \eta||$. The critical buckling length is then dependent on f and on B the bending

modulus. Here the effective drag is defined per length. I can see from this that if the active force is fixed, and the viscous component resulting from the frictional mechanism is fixed, the critical buckling length will not depend on the velocity (unless I am missing something in their argument), since the velocity is not a primitive variable, and is itself an emergent quantity.

Reviewer #2 (Public Review):

In the presented manuscript, the authors first use structured microfluidic devices with gliding filamentous cyanobacteria inside in combination with micropipette force measurements to measure the bending rigidity of the filaments.

Next, they use triangular structures to trap the bacteria with the front against an obstacle. Depending on the length and rigidity, the filaments buckle under the propulsive force of the cells. The authors use theoretical expressions for the buckling threshold to infer propulsive force, given the measured length and stiffnesses. They find nearly identical values for both species, $f \sim (1.0 \pm 0.6) \text{ nN}\mu\text{m}$, nearly independent of the velocity.

Finally, they measure the shape of the filament dynamically to infer friction coefficients via Kirchhoff theory. This last part seems a bit inconsistent with the previous inference of propulsive force. Before, they assumed the same propulsive force for all bacteria and showed only a very weak correlation between buckling and propulsive velocity. In this section, they report a strong correlation with velocity, and report propulsive forces that vary over two orders of magnitude. I might be misunderstanding something, but I think this discrepancy should have been discussed or explained.

From a theoretical perspective, not many new results are presented. The authors repeat the well-known calculation for filaments buckling under propulsive load and arrive at the literature result of buckling when the dimensionless number (fL^3/B) is larger than 30.6 as previously derived by Sekimoto et al in 1995 [1] (see [2] for a clamped boundary condition and simulations). Other theoretical predictions for pushed semi-flexible filaments [1-4] are not discussed or compared with the experiments.

Finally, the Authors use molecular dynamics type simulations similar to [2-4] to reproduce the buckling dynamics from the experiments. Unfortunately, no systematic comparison is performed.

[1] K. Sekimoto, N. Mori, K. Tawada and Y. Toyoshima, Phys. Rev. Lett., 1995, 75, 172-175

[2] R. Chelakkot, A. Gopinath, L. Mahadevan and M. F. Hagan, J. R. Soc., Interface, 2014, 11, 20130884.

[3] R. E. Isele-Holder, J. Elgeti and G. Gompper, Soft Matter, 2015, 11, 7181-7190.

[4] R. E. Isele-Holder, J. Jager, G. Saggiorato, J. Elgeti and G. Gompper, Soft Matter, 2016, 12, 8495

Reviewer #3 (Public Review):

Summary:

This paper presents novel and innovative force measurements of the biophysics of gliding cyanobacteria filaments. These measurements allow for estimates of the resistive force between the cell and substrate and provide potential insight into the motility mechanism of these cells, which remains unknown.

Strengths:

The authors used well-designed microfabricated devices to measure the bending modulus of these cells and to determine the critical length at which the cells buckle. I especially appreciated the way the authors constructed an array of pillars and used it to do 3-point

bending measurements and the arrangement the authors used to direct cells into a V-shaped corner in order to examine at what length the cells buckled at. By examining the gliding speed of the cells before buckling events, the authors were able to determine how strongly the buckling length depends on the gliding speed, which could be an indicator of how the force exerted by the cells depends on cell length; however, the authors did not comment on this directly.

Weaknesses:

There were two minor weaknesses in the paper.

First, the authors investigate the buckling of these gliding cells using an Euler beam model. A similar mathematical analysis was used to estimate the bending modulus and gliding force for *Myxobacteria* (C.W. Wolgemuth, *Biophys. J.* 89: 945-950 (2005)). A similar mathematical model was also examined in G. De Canio, E. Lauga, and R.E Goldstein, *J. Roy. Soc. Interface*, 14: 20170491 (2017). The authors should have cited these previous works and pointed out any differences between what they did and what was done before.

The second weakness is that the authors claim that their results favor a focal adhesion-based mechanism for cyanobacterial gliding motility. This is based on their result that friction and adhesion forces correlate strongly. They then conjecture that this is due to more intimate contact with the surface, with more contacts producing more force and pulling the filaments closer to the substrate, which produces more friction. They then claim that a slime-extrusion mechanism would necessarily involve more force and lower friction. Is it necessarily true that this latter statement is correct? (I admit that it could be, but is it a requirement?)

Related to this, the authors use a model with isotropic friction. They claim that this is justified because they are able to fit the cell shapes well with this assumption. How would assuming a non-isotropic drag coefficient affect the shapes? It may be that it does equally well, in which case, the quality of the fits would not be informative about whether or not the drag was isotropic or not.